Dissipation-Engineered Family of Nearly Dark States in Many-Body Cavity-Atom Systems

Rui Lin,[1] Rodrigo Rosa-Medina,[2] Francesco Ferri,[2] Fabian Finger,[2] Katrin Kroeger,[2] Tobias Donner,[2] Tilman Esslinger,[2] and R. Chitra[1]
[1]*Institute for Theoretical Physics, ETH Zürich, 8093 Zurich, Switzerland*
[2]*Institute for Quantum Electronics, ETH Zürich, 8093 Zurich, Switzerland*

(Received 21 September 2021; accepted 24 February 2022; published 11 April 2022)

Three-level atomic systems coupled to light have the capacity to host dark states. We study a system of V-shaped three-level atoms coherently coupled to the two quadratures of a dissipative cavity. The interplay between the atomic level structure and dissipation makes the phase diagram of the open system drastically different from the closed one. In particular, it leads to the stabilization of a continuous family of dark and nearly dark excited many-body states with inverted atomic populations as the steady states. The multistability of these states can be probed via their distinct fluctuations and excitation spectra, as well as the system's Liouvillian dynamics which are highly sensitive to ramp protocols. Our model can be implemented experimentally by encoding the two higher-energy modes in orthogonal density-modulated states in a bosonic quantum gas. This implementation offers prospects for potential applications like the realization of quantum optical random walks and microscopy with subwavelength spatial resolution.

DOI: 10.1103/PhysRevLett.128.153601

The interaction between matter and light has received enduring attention over decades. Particularly, dark states can be achieved where atoms are decoupled from the light radiation channel. Single particle dark states lie at the core of diverse phenomena and applications like coherent population trapping [1–4], electromagnetically induced transparency [5,6], atomic clocks [7,8], atom cooling [9,10], and slow-light polaritons [11–13]. More recently, many-body dark states have been explored, revealing their importance in quantum information and quantum computation [14–18].

Concurrently, ultracold atomic gases in high-finesse optical cavities have emerged as a versatile platform to simulate hitherto unexplored strongly coupled light-matter phases [19–21]. A paradigmatic example is the realization of the Dicke superradiant phase [22–25] in a weakly interacting Bose-Einstein condensate (BEC) coupled to a cavity [19,26]. The ubiquitous dissipation present in these systems can be exploited to obtain squeezing and entanglement [27], chiral states [28], as well as oscillatory and chaotic dynamics [29–39]. Particularly, cavity dissipation is known to stabilize excited eigenstates as steady states in the interpolating Dicke–Tavis-Cummings (IDTC) model where two-level atoms are coupled to both quadratures of the cavity field [40,41], which has recently been experimentally verified by coupling thermal atoms [42] or a spinor BEC [43] to an optical cavity. An exciting but relatively underexplored frontier in cavity-QED systems is many-body dark-state physics [44–46].

In this Letter, we study a many-body cavity-atom system, where the atomic subspace has an enlarged symmetry, and unveil how dissipative stabilization of excited states fosters the realization of a continuous family of dark and nearly dark steady states with intrinsic many-body correlations. This dark-state preparation is via cavity dissipation in contrast to spontaneous atomic emission [6,47]. To this end, we consider N identical, effective V-shaped three-level atoms coupled to a dissipative cavity with resonance frequency ω and dissipation rate κ in the thermodynamic limit $N \to \infty$ [Fig. 1(a)]. The atoms have two distinct but degenerate levels $|1\rangle$ and $|2\rangle$ separated by an energy ω_0 from the lowest level $|0\rangle$. The transitions between the ground level and the excited levels are exclusively mediated by coherent couplings to the two orthogonal quadratures of the cavity fields with respective strengths λ_1 and λ_2. In atomic gases, such an effective atomic spectrum can be designed by addressing motional degrees of freedom with external laser fields [48–51], or by combining them with internal atomic levels [52]. The Hamiltonian governing this system is given by ($\hbar = 1$)

$$\hat{H} = \omega \hat{a}^\dagger \hat{a} + \omega_0(\hat{\Sigma}_{11} + \hat{\Sigma}_{22}) + \frac{i\lambda_1}{\sqrt{N}}(\hat{a} - \hat{a}^\dagger)(\hat{\Sigma}_{01} + \hat{\Sigma}_{10}) + \frac{i\lambda_2}{\sqrt{N}}(\hat{a} + \hat{a}^\dagger)(\hat{\Sigma}_{02} - \hat{\Sigma}_{20}), \quad (1)$$

where $\hat{a}$ is the cavity annihilation operator, and $\hat{\Sigma}_{\mu\nu} = \sum_{j=1}^{N} |\mu\rangle_j \langle\nu|_j$ are the collective pseudospin operators with $|\mu\rangle_j$ denoting the μth level ($\mu \in \{0, 1, 2\}$) of the jth atom. A similar model has been considered in Ref. [52], which focused on the superradiant features in the low energy sectors.

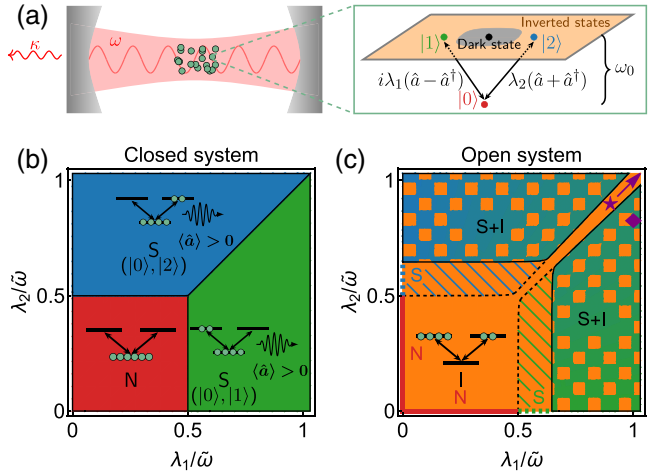

FIG. 1. (a) System schematics illustrating an ensemble of three-level ($|0\rangle$, $|1\rangle$, and $|2\rangle$) atoms with energy splitting ω_0 coupled to an optical cavity $\hat{a}$ with resonance frequency ω and dissipation rate κ through coupling strengths $\lambda_{1,2}$. Also shown is a representation of the inverted states as mixed or superposition states of levels $|1\rangle$ and $|2\rangle$, including the nearly dark (gray region) and the dark (black point) states. (b),(c) Phase diagrams illustrating (b) the ground states for the closed system Eq. (1), and (c) the steady states for the open system Eq. (4). Pictorial representations of the normal (N), superradiant (S), and inverted (I) states are superimposed. In panel (c), the thick solid and dotted lines indicate that the normal and superradiant states are stable only for $\lambda_1 = 0$ or $\lambda_2 = 0$. Superradiant states stably coexist with the inverted states in the tiled regions, and are physical but unstable in the hatched regions. The purple star and diamond indicate the end points of the ramps in Figs. 3 and 4, respectively. System parameters are $\omega = 2\tilde{\omega}$, $\omega_0 = 0.5\tilde{\omega}$, and $\kappa = 0.1\tilde{\omega}$ with reference frequency $\tilde{\omega}$.

The Hamiltonian possesses a $\mathbb{Z}_2 \times \mathbb{Z}_2$ parity symmetry $\Pi = \mathcal{T}_1 \circ \mathcal{T}_2$, where $\mathcal{T}_1$ and $\mathcal{T}_2$ are defined by $(\hat{a}, \hat{\Sigma}_{01}, \hat{\Sigma}_{02}) \overset{\mathcal{T}_1}{\mapsto} (-\hat{a}^\dagger, \hat{\Sigma}_{01}, -\hat{\Sigma}_{02})$ and $(\hat{a}, \hat{\Sigma}_{01}, \hat{\Sigma}_{02}) \overset{\mathcal{T}_2}{\mapsto} (\hat{a}^\dagger, -\hat{\Sigma}_{01}, \hat{\Sigma}_{02})$, and can be broken separately. When $\lambda_1 = \lambda_2$, this symmetry is enlarged to a U(1) symmetry with generator $\mathcal{G} = \hat{a}^\dagger \hat{a} - (\hat{\Sigma}_{12} + \hat{\Sigma}_{21})$. The levels $|1\rangle$ and $|2\rangle$ have completely equivalent roles in the Hamiltonian. The pseudospin operators $\hat{\Sigma}_{\mu\nu}$ follow the commutation relation of the Gell-Mann matrices and, thus, span an SU(3) symmetry space [see Supplemental Material (SM) [53]]. In comparison, a spin-one implementation with SU(2) symmetry [63] realizes an equally spaced Ξ-shaped three-level system, where the middle level is equally coupled to the upper and lower ones [53]. This is qualitatively different from our V-shaped system.

The closed system phase diagram of our system as summarized in Fig. 1(b) and the corresponding polaritonic excitation spectra can be obtained by using an SU(3) generalization of the Holstein-Primakoff transformation [53,64]. For small couplings $\lambda \equiv \max(\lambda_1, \lambda_2) < \lambda_c = \frac{1}{2}\sqrt{\omega\omega_0}$, the system stays in the normal phase with an empty cavity and all atoms populating the $|0\rangle$ level. When either coupling exceeds the threshold $\lambda > \lambda_c$, the system enters the superradiant phase where the cavity field is coherently populated as $|\langle\hat{a}\rangle| = (\lambda\sqrt{N}/\omega)\sqrt{1-(\omega_0\omega/4\lambda^2)^2}$. For $\lambda_1 > \lambda_2$ ($\lambda_2 > \lambda_1$), the $\mathcal{T}_1$ ($\mathcal{T}_2$) symmetry is spontaneously broken, leading to a nonzero expectation value of the imaginary (real) quadrature of the cavity field and an occupation of the $|0\rangle$ and $|1\rangle$ ($|2\rangle$) levels. For $\lambda_1 = \lambda_2 > \lambda_c$, the broken U(1) symmetry results in a population of all three atomic levels.

In the high-energy sector, our model hosts a dark state decoupled from the cavity field and, thus, is stable, obeying $\hat{H}|D\rangle = N\omega_0|D\rangle$ and $\hat{a}|D\rangle = 0$ [65–67]

$$|D\rangle = \prod_{j=1}^{N} \frac{\lambda_2|1\rangle_j + \lambda_1|2\rangle_j}{\sqrt{\lambda_1^2 + \lambda_2^2}}. \tag{2}$$

This state manifests a complete atomic population inversion with unoccupied $|0\rangle$ level. In fact, it is merely one element of a family of states satisfying $\langle\hat{\Sigma}_{0\nu}\rangle = 0$ and $\langle\hat{a}\rangle = 0$ in $\mathcal{O}(N)$, which we term the inverted states. These states are uniquely defined by two parameters,

$$N_1 = \langle\hat{\Sigma}_{11}\rangle, \qquad \theta = \arg\langle\hat{\Sigma}_{12}\rangle, \tag{3}$$

where $N_1 \in [0, N]$ is the occupation of level $|1\rangle$, and $\theta \in (-\pi, \pi]$ is the relative phase between levels $|1\rangle$ and $|2\rangle$. These quasidegenerate inverted states have a much higher energy $E = N\omega_0$ compared to the polaritonic excitations, whose energy is in $\mathcal{O}(1)$ [53]. These states stem from the enlarged SU(3) symmetry and, in contrast to the dark state of Eq. (2), are characterized by nontrivial many-body correlations. Despite the inaccessibility of these inverted states with quasiadiabatic protocols in the closed system, they are inherently related to the dark state upon introduction of dissipation.

Now, we explicitly consider cavity dissipation via a Liouvillian time evolution of the density matrix [68]

$$\partial_t\hat{\rho} = \mathcal{L}\hat{\rho} = -i[\hat{H}, \hat{\rho}] + \kappa(2\hat{a}\,\hat{\rho}\,\hat{a}^\dagger - \{\hat{a}^\dagger\hat{a}, \hat{\rho}\}). \tag{4}$$

The stability of the Liouvillian's fixed points determines the steady states of the system. In the third quantization approach [69,70], this can be inferred from rapidities $\{\xi_i\}$, whose construction and calculation from the Liouvillian are detailed in the SM [53]. The values of ξ_i dictate the stability of the steady states to fluctuations. A state is stable (unstable) when $\mathrm{Re}\xi_{\min} \geq 0$ ($\mathrm{Re}\xi_{\min} < 0$), with $\xi_{\min}$ the rapidity with the minimal real part. The system converges to (deviates from) it with a rate of $2|\mathrm{Re}\xi_{\min}|$ and an oscillation frequency of $2|\mathrm{Im}\xi_{\min}|$ [69,70]. As detailed in the SM [53], although the normal, superradiant, and inverted states all remain fixed points of the Liouvillian [Eq. (4)], their stabilities are dramatically altered by

dissipation. The resulting open system stability diagram is summarized in Fig. 1(c). Without loss of generality, we assume $\lambda_1 \geq \lambda_2$ in the following discussion.

The first intriguing aspect of the open system is the generic instability of the normal state, which is now stable only when $\lambda_2 = 0$ recovering the Dicke model, and $\lambda_1 < \frac{1}{2}\sqrt{(\omega^2+\kappa^2)\omega_0/\omega}$ [52]. Dissipation also significantly impacts the superradiant states, where all atomic levels are now populated. At the level of fixed points, akin to the IDTC model [40], the U(1) symmetry broken phase at $\lambda_1 = \lambda_2$ is eliminated, and two superradiant boundaries separated by a sliver emerge symmetric about $\lambda_1 = \lambda_2$. Each superradiant boundary harbors both continuous and first order sections [53]. In contrast to the IDTC model, the superradiant state is unstable in an intermediate region above the critical coupling of the closed system [hatched region in Fig. 1(c)], as inferred from the associated rapidities [53]. This superradiant state stability boundary is almost insensitive to the weaker coupling, and lies where the stronger coupling λ_1 takes the approximate value of

$$\lambda_{\text{stable}} \approx \sqrt{(\omega^2+\kappa^2)(\omega+2\sqrt{4\omega^2+3\kappa^2})\omega_0/12\omega^2}. \tag{5}$$

Both normal and superradiant states manifest mathematical singularity in fluctuations in both limits $\lambda_2 \to 0$ and $\kappa \to 0$ [53]. A slight deviation from the Dicke model together with an infinitesimal dissipation immediately destabilizes the superradiant state when $1 \leq \lambda_1/\lambda_c \lesssim \sqrt{5/3}$ and the normal state.

The high-energy inverted states show a nontrivial stability, as only a subset of them is stable. In the N_1-θ parameter space, the inverted state stability boundary as depicted in Fig. 2(a) is given by

$$\frac{\eta_1\eta_2\cos\theta}{\eta_1^2+\eta_2^2} = \frac{\omega\omega_0}{\omega^2+\omega_0^2+\kappa^2} \equiv \Omega, \tag{6}$$

where $\eta_1 = \lambda_1\sqrt{N_1/N}$, $\eta_2 = \lambda_2\sqrt{1-N_1/N}$, and $\Omega \in (0, 1/2)$ is a scaled variable. The enclosed extended region of multistability has a finite area $A = N\pi[1-\Omega(\lambda_1^2+\lambda_2^2)/\sqrt{\lambda_1^2\lambda_2^2+(\lambda_1^2-\lambda_2^2)^2\Omega^2}]$, which increases for less resonant ω and ω_0, and for larger κ. Consistently, the dark state $|D\rangle$ introduced in Eq. (2) corresponds to $(N_1, \theta) = (N\lambda_2^2/(\lambda_1^2+\lambda_2^2), 0)$, and always lies inside the stable region for all values of Ω. These nearly dark inverted states are either the exclusive steady states [orange region in Fig. 1(c)] or coexistent with superradiant states [hatched regions in Fig. 1(c)]. We reiterate that such multistable steady states cannot be realized using SU(2) atoms with cavity modes coupled linearly to it (see SM [53]), which can host only one coherent dark state [45,46]. Indeed, their realization requires a larger atomic symmetry like SU(3) [53], and has been predicted in an SU(3) atomic system coupled to two cavity modes [44]. Moreover, their existence and population inversion further requires both the degeneracy of the levels $|1\rangle$ and $|2\rangle$ and a positive ω_0 as well. For $\omega_0 < 0$, a similar family of nearly dark states exists albeit without population inversion (see SM [53]). An in-depth exploration beyond these parameter regimes merits future study.

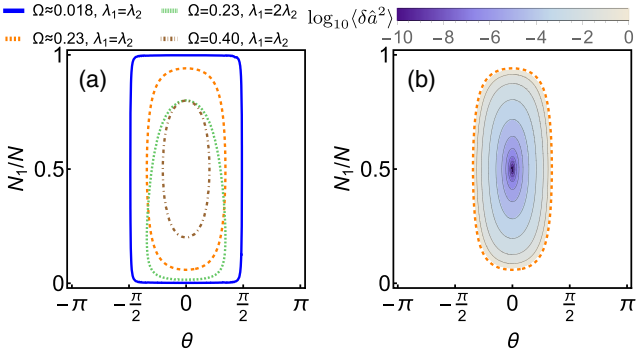

FIG. 2. (a) Stability boundaries of the inverted state in the open system for different system parameters given by Eq. (6). The regions enclosed indicate stable solutions. The boundary is only sensitive to the coupling ratio λ_1/λ_2 and the scale variable Ω. The blue solid line corresponds to typical experimental parameters $\omega = 2\pi \times 2.0$ MHz, $\omega_0 = 2\pi \times 50$ kHz, and $\kappa = 2\pi \times 1.25$ MHz [43,49], the orange dashed line and green dotted line correspond to the parameters used in Fig. 1: $\omega = 2\tilde{\omega}$, $\omega_0 = 0.5\tilde{\omega}$, and $\kappa = 0.1\tilde{\omega}$, whereas the brown dash-dotted line depicts a scenario with larger $\Omega = 0.4$. (b) Cavity field fluctuations $\langle\delta\hat{a}^2\rangle$ [cf. Eq. (7)] of different inverted states in the stable region, with system parameters taken as $\omega = 2\tilde{\omega}$, $\omega_0 = 0.5\tilde{\omega}$, $\kappa = 0.1\tilde{\omega}$, and $\lambda_1 = \lambda_2 = \tilde{\omega}$.

To distinguish between the inverted states, a direct measurement of the atomic observables N_1 and θ can be experimentally challenging. An alternative is to extract the cavity and atomic fluctuations as well as the excitation spectra harbored by the individual states. Particularly, the cavity fluctuations $\langle\delta\hat{a}^2\rangle \equiv \langle\hat{a}^\dagger\hat{a}\rangle - |\langle\hat{a}\rangle|^2$ are found to be [53]

$$\langle\delta\hat{a}^2\rangle = \frac{(\eta_1^4+\eta_2^4-2\eta_1^2\eta_2^2\cos 2\theta)(\omega^2+\kappa^2+4\eta_1\eta_2\cos\theta)\omega_0^2}{2[8\eta_1^2\eta_2^2(1+\cos 2\theta)+4(\eta_1^2+\eta_2^2)\omega\omega_0+(\omega^2+\kappa^2)\omega_0^2][\eta_1\eta_2(\omega^2+\omega_0^2+\kappa^2)\cos\theta-(\eta_1^2+\eta_2^2)\omega\omega_0]}, \tag{7}$$

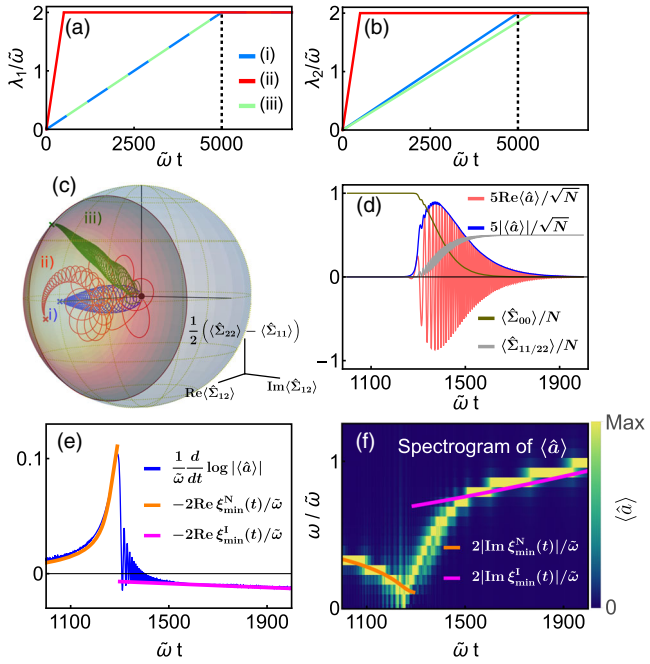

FIG. 3. Dynamical evolution probing the multistability of the inverted states. (a),(b) The time dependence of (a) $\lambda_1(t)$ and (b) $\lambda_2(t)$ in the three protocols [53]. (c) The trajectories of all three protocols projected on the Bloch sphere spanned by $|1\rangle$ and $|2\rangle$. The black dot indicates the starting point of the trajectories, i.e., the normal state, while the crosses indicate the final points. The stable region of the inverted states, appearing as the colored spherical cap in this representation [53], corresponds to the one shown in Fig. 2(b). (d) Evolution of the cavity and atomic fields during the pulse in protocol (i), where (e),(f) the simulated dynamics quantitatively agrees with the theoretically calculated rapidities $\xi^{\mathrm{N}}_{\mathrm{min}}$ for the normal state and $\xi^{\mathrm{I}}_{\mathrm{min}}$ for the inverted state with $(N_1,\theta)=(1/2,0)$ evaluated with instantaneous coupling strengths. Particularly, (e) the time derivative of $|\langle\hat{a}\rangle|$ depicting the deviation or convergence rate quantitatively agree with $\mathrm{Re}\xi_{\mathrm{min}}$, whereas (f) the spectrogram of $\langle\hat{a}\rangle$ depicting the oscillation frequency to $\mathrm{Im}\xi_{\mathrm{min}}$.

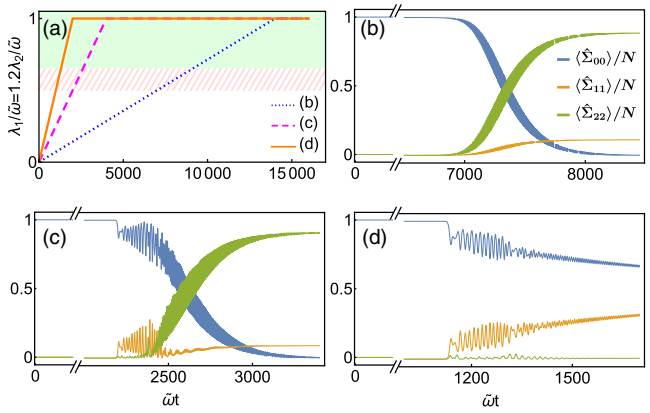

FIG. 4. Dynamical evolution probing the accessibility of the superradiant states. (a) The ramp protocols of the coupling strengths [53]. The regions in which the superradiant state is unstable, stable, and unphysical for the corresponding instantaneous coupling strengths are marked in green, hatched red, and white, respectively, cf. Fig. 1(c). (b)–(d) Qualitatively different evolutions of the atomic fields for the three protocols.

and vary over orders of magnitude within the stable region, diverging at the stability boundary and strongly suppressed around $|D\rangle$ [Fig. 2(b)]. The vanishing cavity and atomic fluctuations at $|D\rangle$ corroborate its darkness and atomic coherence, whereas the states in its vicinity are mixed states with intrinsic many-body correlations and finite fluctuations. Measurements of the cavity fluctuations and the excitation spectra can uniquely determine the inverted state for unequal couplings $\lambda_1\neq\lambda_2$, but only up to a closed contour in the N_1-θ parameter space for equal couplings $\lambda_1=\lambda_2$, as is consistent with the U(1) symmetry [53].

The full Liouvillian dynamics of the system can be captured by numerically solving the coupled mean-field equations of motion for the cavity and atomic fields, using the normal state with a small cavity field as the initial state, and different time-dependent ramp protocols for the two couplings. These are seven coupled complex equations governing the expectation values of $\langle\hat{a}\rangle$, $\langle\hat{\Sigma}_{01}\rangle$, $\langle\hat{\Sigma}_{02}\rangle$, $\langle\hat{\Sigma}_{12}\rangle$, $\langle\hat{\Sigma}_{00}\rangle$, $\langle\hat{\Sigma}_{11}\rangle$, and $\langle\hat{\Sigma}_{22}\rangle$ [53]. As a representative case, the system parameters are chosen as $\omega=2\tilde{\omega}$, $\omega_0=0.5\tilde{\omega}$, and $\kappa=0.1\tilde{\omega}$ with reference frequency $\tilde{\omega}$.

We ramp up the couplings from $\lambda_1=\lambda_2=0$ to $\lambda_1=\lambda_2=2\tilde{\omega}$ using three different protocols as illustrated in Figs. 3(a) and 3(b), which differ in ramp rate and path in λ_1-λ_2 parameter space. For a better visualization, the ensuing Liouvillian trajectories are projected onto the Bloch sphere spanned by the axes $\mathrm{Re}\langle\hat{\Sigma}_{12}\rangle$, $\mathrm{Im}\langle\hat{\Sigma}_{12}\rangle$, and $\frac{1}{2}(\langle\hat{\Sigma}_{22}\rangle-\langle\hat{\Sigma}_{11}\rangle)$ [Fig. 3(c)]. Despite identical final couplings, the final converged state depends sensitively on both ramp rate and path, signaling the multistability of the inverted states. The nature of the dynamics is further elucidated by studying the cavity field evolution. As the atomic population inverts, correlations between atomic levels $\langle\hat{\Sigma}_{01}\rangle$ and $\langle\hat{\Sigma}_{02}\rangle$ are established. This automatically generates a nonzero $\langle\hat{a}\rangle$ signifying a burst of photons [Fig. 3(d)]. We can best understand this in the bad-cavity limit $\kappa\gg\omega_0$, where the cavity field follows the atomic evolution adiabatically as $\langle\hat{a}\rangle=(i\lambda_1\mathrm{Re}\langle\hat{\Sigma}_{01}\rangle+\lambda_2\mathrm{Im}\langle\hat{\Sigma}_{02}\rangle)/[\sqrt{N}(\omega+i\kappa)]$. The quantitative consistency between cavity field dynamics and rapidities [Figs. 3(e) and 3(f)] confirms the dissipative nature of the instability driving the population inversion.

Now, we discuss the accessibility of the superradiant steady states by considering three ramp protocols satisfying $\lambda_1/\lambda_2=1.2$ [Fig. 4(a)]. They traverse the unstable superradiant region and terminate in the region where both the superradiant and the inverted states are stable [purple diamond in Fig. 1(c)]. We find a ramp-dependent dynamics mirroring the complex stability of the states, as shown in Fig. 4. For the slowest ramp [Fig. 4(b)], the dynamics is

dominated by the instability of the normal state to the inverted state. For an intermediate ramp rate [Fig. 4(c)], the system first enters the unstable superradiant state before being driven by its instability to the inverted state. Finally, for a fast enough ramp [Fig. 4(d)], the system is quenched to the stable superradiant state before it can invert toward the nearly dark states.

Our model can be experimentally implemented using a two-dimensional BEC in the x-z plane with effectively two internal Zeeman sublevels $|m=0\rangle$ and $|m=1\rangle$ coupled to a dissipative cavity with typical parameters of $\omega = 2\pi \times 2.0$ MHz and $\kappa = 2\pi \times 1.25$ MHz, and driven by a bichromatic laser whose two standing-wave modulations are phase shifted by $\pi/2$ at the position of the atomic cloud [49]. To the lowest order in kinetic energy, this atomic system can be effectively mapped to our model [Eq. (1)], where $|0\rangle$ corresponds to a spatially uniform state $\psi_0 \propto |m=0\rangle \otimes 1$, while $|1\rangle$ and $|2\rangle$ are orthogonal spatially modulated modes with wave vector k: $\psi_1 \propto |m=1\rangle \otimes \cos(kx)\cos(kz)$ and $\psi_2 \propto |m=1\rangle \otimes \cos(kx)\sin(kz)$, respectively. This implementation structurally protects the degeneracy of the $|1\rangle$ and $|2\rangle$ levels. The energy difference ω_0 between the atomic levels is contributed by both the Zeeman splitting and the recoil energy and has a typical value of $\omega_0 = 2\pi \times 50$ kHz. Controlled by the pump laser, the couplings λ_1 and λ_2 take values in the range of $2\pi \times 100$ kHz. For these experimentally associated parameters, the inverted state stability boundary in N_1-θ parameter space is plotted as the blue solid curve in Fig. 2(a), showing a vast multistable region and, thus, indicating an easy observability of our predicted results. Other proposed experimental realizations of similar models are also discussed in Refs. [51,52].

In conclusion, the dissipative stabilization of a continuous family of excited many-body states as steady states establishes a new paradigm for preparing nearly dark states in cavity-atom systems. These salient features pave the way for a wide range of prospective applications. For instance, the large multistable region provides a potential platform for implementing fluctuation-driven random walks like Lévy flight [71], which can be used for atom cooling [72–74]. Moreover, in the experimental implementation discussed above [49], the established correspondence between matter and light can potentially be used for fluctuation-based microscopy of the atomic density patterns with subwavelength resolution [75].

We are grateful to M. Landini, N. Dogra, A. U. J. Lode, and O. Zilberberg for fruitful discussions. R. L. and R. C. acknowledge funding from the ETH grants. R. R.-M., F. Ferri, F. Finger, T. D., and T. E. acknowledge funding from the Swiss National Science Foundation: Projects No. 182650 and No. 175329 (NAQUAS QuantERA) and NCCR QSIT (No. 51NF40-185902), from EU Horizon2020: ERC Advanced Grant TransQ (Project No. 742579).

[1] E. Arimondo and G. Orriols, Lett. Nuovo Cimento Soc. Ital. Fis. **17**, 333 (1976).
[2] P. M. Radmore and P. L. Knight, J. Phys. B **15**, 561 (1982).
[3] K. Bergmann, H. Theuer, and B. W. Shore, Rev. Mod. Phys. **70**, 1003 (1998).
[4] E. Arimondo, *Progress in Optics* (Elsevier, New York, 1996), Vol. 35, pp. 257–354.
[5] K.-J. Boller, A. Imamoğlu, and S. E. Harris, Phys. Rev. Lett. **66**, 2593 (1991).
[6] M. Fleischhauer, A. Imamoglu, and J. P. Marangos, Rev. Mod. Phys. **77**, 633 (2005).
[7] J. Vanier, Appl. Phys. B **81**, 421 (2005).
[8] V. Shah and J. Kitching, in *Advances in Atomic, Molecular, and Optical Physics*, edited by E. Arimondo, P. R. Berman, and C. C. Lin (Academic Press, New York, 2010), Vol. 59, pp. 21–74.
[9] A. Aspect, E. Arimondo, R. Kaiser, N. Vansteenkiste, and C. Cohen-Tannoudji, Phys. Rev. Lett. **61**, 826 (1988).
[10] G. Morigi, J. Eschner, and C. H. Keitel, Phys. Rev. Lett. **85**, 4458 (2000).
[11] M. Fleischhauer and M. D. Lukin, Phys. Rev. A **65**, 022314 (2002).
[12] C. Kupchak, T. Mittiga, B. Jordaan, M. Namazi, C. Nölleke, and E. Figueroa, Sci. Rep. **5**, 7658 (2015).
[13] F. Grusdt and M. Fleischhauer, Phys. Rev. Lett. **116**, 053602 (2016).
[14] K. Stannigel, P. Rabl, and P. Zoller, New J. Phys. **14**, 063014 (2012).
[15] H. Pichler, T. Ramos, A. J. Daley, and P. Zoller, Phys. Rev. A **91**, 042116 (2015).
[16] G. Buonaiuto, R. Jones, B. Olmos, and I. Lesanovsky, New J. Phys. **21**, 113021 (2019).
[17] T. Pistorius, J. Kazemi, and H. Weimer, Phys. Rev. Lett. **125**, 263604 (2020).
[18] S. H. Cantu, A. V. Venkatramani, W. Xu, L. Zhou, B. Jelenković, M. D. Lukin, and V. Vuletić, Nat. Phys. **16**, 921 (2020).
[19] K. Baumann, C. Guerlin, F. Brennecke, and T. Esslinger, Nature (London) **464**, 1301 (2010).
[20] H. Ritsch, P. Domokos, F. Brennecke, and T. Esslinger, Rev. Mod. Phys. **85**, 553 (2013).
[21] F. Mivehvar, F. Piazza, T. Donner, and H. Ritsch, Adv. Phys. **70**, 1 (2021).
[22] R. H. Dicke, Phys. Rev. **93**, 99 (1954).
[23] K. Hepp and E. H. Lieb, Ann. Phys. (N.Y.) **76**, 360 (1973).
[24] H. Wang and M. Thoss, New J. Phys. **10**, 115005 (2008).
[25] H. Carmichael, C. Gardiner, and D. Walls, Phys. Lett. **46A**, 47 (1973).
[26] J. Klinder, H. Keßler, M. R. Bakhtiari, M. Thorwart, and A. Hemmerich, Phys. Rev. Lett. **115**, 230403 (2015).
[27] B. Buča and D. Jaksch, Phys. Rev. Lett. **123**, 260401 (2019).
[28] N. Dogra, M. Landini, K. Kroeger, L. Hruby, T. Donner, and T. Esslinger, Science **366**, 1496 (2019).
[29] F. Piazza and H. Ritsch, Phys. Rev. Lett. **115**, 163601 (2015).
[30] P. Molignini, L. Papariello, A. U. J. Lode, and R. Chitra, Phys. Rev. A **98**, 053620 (2018).

[31] F. Iemini, A. Russomanno, J. Keeling, M. Schirò, M. Dalmonte, and R. Fazio, Phys. Rev. Lett. **121**, 035301 (2018).

[32] E. I. Rodriguez Chiacchio and A. Nunnenkamp, Phys. Rev. Lett. **122**, 193605 (2019).

[33] R. Lin, P. Molignini, A. U. J. Lode, and R. Chitra, Phys. Rev. A **101**, 061602(R) (2020).

[34] H. Keßler, J. G. Cosme, M. Hemmerling, L. Mathey, and A. Hemmerich, Phys. Rev. A **99**, 053605 (2019).

[35] P. Zupancic, D. Dreon, X. Li, A. Baumgärtner, A. Morales, W. Zheng, N. R. Cooper, T. Esslinger, and T. Donner, Phys. Rev. Lett. **123**, 233601 (2019).

[36] H. Keßler, J. G. Cosme, C. Georges, L. Mathey, and A. Hemmerich, New J. Phys. **22**, 085002 (2020).

[37] K. C. Stitely, A. Giraldo, B. Krauskopf, and S. Parkins, Phys. Rev. Research **2**, 033131 (2020).

[38] H. Keßler, P. Kongkhambut, C. Georges, L. Mathey, J. G. Cosme, and A. Hemmerich, Phys. Rev. Lett. **127**, 043602 (2021).

[39] L. F. d. Prazeres, L. d. S. Souza, and F. Iemini, Phys. Rev. B **103**, 184308 (2021).

[40] M. Soriente, T. Donner, R. Chitra, and O. Zilberberg, Phys. Rev. Lett. **120**, 183603 (2018).

[41] M. Soriente, T. L. Heugel, K. Omiya, R. Chitra, and O. Zilberberg, Phys. Rev. Research **3**, 023100 (2021).

[42] Z. Zhang, C. H. Lee, R. Kumar, K. J. Arnold, S. J. Masson, A. L. Grimsmo, A. S. Parkins, and M. D. Barrett, Phys. Rev. A **97**, 043858 (2018).

[43] F. Ferri, R. Rosa-Medina, F. Finger, N. Dogra, M. Soriente, O. Zilberberg, T. Donner, and T. Esslinger, Phys. Rev. X **11**, 041046 (2021).

[44] M. Hayn, C. Emary, and T. Brandes, Phys. Rev. A **84**, 053856 (2011).

[45] C. Emary, J. Phys. B **46**, 224008 (2013).

[46] E. G. Dalla Torre, J. Otterbach, E. Demler, V. Vuletic, and M. D. Lukin, Phys. Rev. Lett. **110**, 120402 (2013).

[47] A. Aspect, E. Arimondo, R. Kaiser, N. Vansteenkiste, and C. Cohen-Tannoudji, J. Opt. Soc. Am. B **6**, 2112 (1989).

[48] X. Li, D. Dreon, P. Zupancic, A. Baumgärtner, A. Morales, W. Zheng, N. R. Cooper, T. Donner, and T. Esslinger, Phys. Rev. Research **3**, L012024 (2021).

[49] R. Rosa-Medina, F. Ferri, F. Finger, N. Dogra, K. Kroeger, R. Lin, R. Chitra, T. Donner, and T. Esslinger, Phys. Rev. Lett. **128**, 143602 (2022).

[50] J. Skulte, P. Kongkhambut, H. Keßler, A. Hemmerich, L. Mathey, and J. G. Cosme, Phys. Rev. A **104**, 063705 (2021).

[51] P. Kongkhambut, H. Keßler, J. Skulte, L. Mathey, J. G. Cosme, and A. Hemmerich, Phys. Rev. Lett. **127**, 253601 (2021).

[52] J. Fan, G. Chen, and S. Jia, Phys. Rev. A **101**, 063627 (2020).

[53] See Supplemental Material http://link.aps.org/supplemental/10.1103/PhysRevLett.128.153601, which includes Refs. [54–62], for a discussion on the symmetry of the system, the derivation of Holstein-Primakoff transformation in closed and open systems, the calculation of excitation spectra, rapidities, and fluctuations, the Liouvillian dynamical evolution, the relation between the atomic symmetry and the multistability, and the consequences of modifications of the model.

[54] C. Emary and T. Brandes, Phys. Rev. E **67**, 066203 (2003).

[55] A. Baksic and C. Ciuti, Phys. Rev. Lett. **112**, 173601 (2014).

[56] J. J. Hopfield, Phys. Rev. **112**, 1555 (1958).

[57] M.-W. Xiao, arXiv:0908.0787.

[58] C. W. Gardiner and M. J. Collett, Phys. Rev. A **31**, 3761 (1985).

[59] B. Öztop, M. Bordyuh, O. E. Müstecaplıoğlu, and H. E. Türeci, New J. Phys. **14**, 085011 (2012).

[60] D. Nagy, G. Kónya, G. Szirmai, and P. Domokos, Phys. Rev. Lett. **104**, 130401 (2010).

[61] F. Le Kien, P. Schneeweiss, and A. Rauschenbeutel, Eur. Phys. J. D **67**, 92 (2013).

[62] M. Landini, N. Dogra, K. Kroeger, L. Hruby, T. Donner, and T. Esslinger, Phys. Rev. Lett. **120**, 223602 (2018).

[63] Z. Zhiqiang, C. H. Lee, R. Kumar, K. J. Arnold, S. J. Masson, A. S. Parkins, and M. D. Barrett, Optica **4**, 424 (2017).

[64] M. Wagner, Phys. Lett. **53A**, 1 (1975).

[65] B. Kraus, H. P. Büchler, S. Diehl, A. Kantian, A. Micheli, and P. Zoller, Phys. Rev. A **78**, 042307 (2008).

[66] S. Diehl, A. Micheli, A. Kantian, B. Kraus, H. P. Büchler, and P. Zoller, Nat. Phys. **4**, 878 (2008).

[67] D. Finkelstein-Shapiro, S. Felicetti, T. Hansen, T. o. Pullerits, and A. Keller, Phys. Rev. A **99**, 053829 (2019).

[68] F. Dimer, B. Estienne, A. S. Parkins, and H. J. Carmichael, Phys. Rev. A **75**, 013804 (2007).

[69] T. Prosen, New J. Phys. **10**, 043026 (2008).

[70] T. Prosen and T. H. Seligman, J. Phys. A **43**, 392004 (2010).

[71] P. Lévy, *Théorie de l'Addition des Variables Aléatoires* (Gauthier-Villars, Paris, 1954).

[72] E. Bertin and F. Bardou, Am. J. Phys. **76**, 630 (2008).

[73] F. Bardou, J.-P. Bouchaud, A. Aspect, and C. Cohen-Tannoudji, *Lévy Statistics and Laser Cooling: How Rare Events Bring Atoms to Rest* (Cambridge University Press, Cambridge, England, 2001).

[74] E. G. Rocha, E. P. Santos, B. J. dos Santos, S. S. de Albuquerque, P. I. R. Pincheira, C. Argolo, and A. L. Moura, Phys. Rev. A **101**, 023820 (2020).

[75] A. Neice, *Advances in Imaging and Electron Physics* (Elsevier, New York, 2010), Vol. 163, pp. 117–140.